

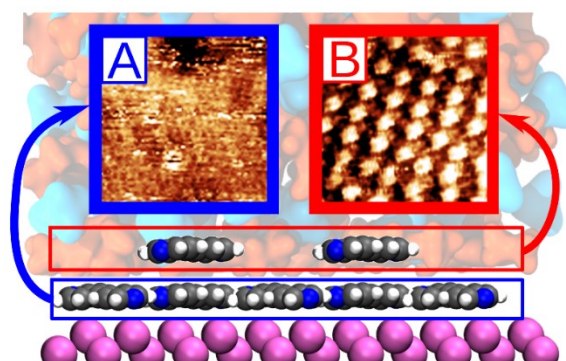
Order beyond a monolayer: the story of two self-assembled 4,4'-bipyridine layers on the Sb(111) | ionic liquid interface

Heigo Ers, Liis Siinor, Carolin Siimenson, Enn Lust, Piret Pikma

Institute of Chemistry, University of Tartu, Ravila 14A, 50411 Tartu, Estonia

Corresponding authors e-mails: piret.pikma@ut.ee

The interface between semi-metallic Sb(111) electrode and ionic liquid with 4,4'-bipyridine addition has been studied. Using *in situ* scanning tunnelling microscopy and electrochemical impedance spectroscopy, the desorption of 4,4'-bipyridine was demonstrated and a dense underlying structure, formed below



a sparse self-assembled monolayer, was visualized. The first SAM layer in contact with the electrode consisted of tightly packed ordered rows, which fine structure has been identified with density functional theory calculations supported by machine learning. The second SAM layer, on top of the first, is characterised by low surface concentration and its unit cell was obtained experimentally. The detection of two separate adsorbed layers indicates that the ordering of organic molecules could extend well beyond the monolayer on the electrode's surface. These insights are of fundamental and practical importance in the development of nanoelectronic devices.

Introduction

Highly organised self-assembled monolayers (SAMs) with controllable properties have had significant attention due to their numerous potential applications^{1,2}. Depending on the chemical and physical properties of the SAMs, they have been used as protective coatings^{3,4} and for the fabrication of organic thin-film transistors and sensors^{2,5,6}. The properties of SAM are governed by the characteristics of individual molecules in the monolayer, by the interactions between these molecules with the surface and themselves, and by SAM interactions with the electrolyte and non-adsorbed organic molecules^{7,8}. Also, as the SAM molecules are adsorbed, the crystalline surface of the substrate has a significant impact on the arrangement of SAM molecules on its surface.

The adsorption of SAMs allows tuning the surface properties such as work function⁹ and wettability¹⁰. Particular interest has been turned to rigid molecules with conjugated backbones, which are characterised by lower tunnel barriers at the interface¹¹. The adsorption of 4,4'-bipyridine (4,4'-BP) contains both π electronic system and nitrogen atoms with lone electron pairs, which facilitate the possibility to bond with the metal surface and other molecules in different ways. Studying the arrangement of 4,4'-BP, therefore, offers a fundamental insight into the competing interactions, which control the structure of SAM. Previously, the 4,4'-BP adsorption has been mostly investigated from aqueous solutions using experimental techniques such as electrochemical impedance spectroscopy (EIS), scanning tunnelling microscopy (STM), infrared and Raman spectroscopy for Au(111)¹², Bi(111)¹³, Cu(111)¹⁴, Sb(111)¹⁵ and Cd(0001)¹⁶ surface. Regardless of the influence of electrolyte, electrode or applied potential, in all aforementioned studies, 4,4'-BP has been shown to form an ordered 2D structures on the electrode surface. Depending on the studied metal monocrystal surface structure, it was demonstrated that 4,4'-BP could adsorb at different orientations: with N atom oriented towards the surface (Au(111), Cd(0001)), with pyridine rings parallel (Cu(111), Sb(111)) and perpendicular (Cu(111), Bi(111)) to the surface, highlighting the effect of metal substrate crystal structure on the SAM structure. The influence of the used electrolyte to the SAM characteristics was shown on Bi(111) electrode, by studying the 4,4'-BP adsorption from weakly acidified Na₂SO₄ aqueous solutions¹³.

The bulk and interfacial properties of room temperature ionic liquids (ILs) have been the subject of numerous studies since 1990s^{17–27}. This considerable interest has been carried by their unique properties such as good thermal and electrochemical stability, low vapour pressure and high viscosity, which allow to consider them as possible lubricants^{28,29}, electrolytes for energy storage devices, *e.g.* fuel cells and supercapacitors^{30,31} and solvents for liquid-phase extraction³². As the properties of ILs differ notably from other organic solvents or water, studying IL solutions, which contain inorganic ions, organic additives or other ILs, can offer fundamental insight into processes occurring at the interface by investigating them within a wider potential region than possible in other solvents or tune the properties of electrode | electrolyte interface for a given task.^{33–35}

In this work, we investigated the adsorption of 4,4'-BP from 1-ethyl-3-methylimidazolium tetrafluoroborate (EMImBF₄) IL at Sb(111) electrode. The main aim was to compare the adsorption characteristics of 4,4'-BP with data from other previously studied 4,4'-BP aqueous and IL electrolyte interfaces with single crystal metal electrodes. Furthermore, as SAMs are

considered for different applications such as corrosion protection and nanoelectronics, it is vital to study the fundamental aspects driving the formation of SAM at different metal electrodes. Semimetallic Sb(111), with a rhombohedral crystal structure that consists of stacked bilayers, was chosen due to its unique electronic properties³⁶ and good stability³⁴ when forming the interface with EMImBF₄ as an electrolyte.

Experimental

To prepare the investigated IL solutions, we used EMImBF₄ (Sigma-Aldrich, for electrochemistry, purity $\geq 99.0\%$, ≤ 200 ppm water) and 4,4'-BP (Thermo Scientific Acros, purity 98.0%, anhydrous). The solutions were prepared in the glovebox ($\text{H}_2\text{O} < 0.3$ ppm, $\text{O}_2 < 0.2$ ppm). All measurements were carried out in a three-electrode electrochemical cell, which consisted of an Sb(111) single crystal plane (Mateck) as working electrode, platinum (Pt) net as counter electrode, and silver chloride (Ag|AgCl) as reference electrode in the glovebox. Electrochemical polishing of Sb(111) surface before each EIS experiment was conducted in saturated KI (Sigma-Aldrich, BioUltra, purity $\geq 99.5\%$) + 0.5% HCl (Merck, Suprapur, 30% solution) aqueous solution at a current densities $j \approx 1.0 \text{ A/cm}^2$. In the case of *in situ* STM experiments, the surface was cleaved. Autolab PGSTAT204 with FRA32M EIS module and Nova 1.10 software package were used for the cyclic voltammetry (CV) and EIS measurements. The frequency range applied in EIS measurements was from 0.1 Hz to 10000 Hz with a step of 15 frequencies per decade. For excitations, a single sine wave with an amplitude of 0.005 V was used. Interfacial capacitance (C) was estimated using relation $C = -(Z''2\pi f)^{-1}$ under the assumption of a non-compensated resistance R and a capacitor C in series. After electrochemical polishing, the working electrode was introduced into the solution at potential $E = -0.6 \text{ V}$.

The *in situ* STM measurements were conducted using a PicoSPMTM molecular imaging system in the constant current mode. The measurements were carried out in argon atmosphere (5.0 Linde Gas), using STM tips that were prepared by electrochemically etching tungsten wire with 5 M KOH (Sigma-Aldrich, puriss. p.a.) solution and later insulated with ApiezonTM wax coating. Insulated STM measuring tip was inserted into the IL solution at $E = -0.7 \text{ V}$. The postprocessing of measured STM images were done using Gwyddion data visualisation and analysis software³⁷.

Calculations

To estimate the most probable configurations of the dense 4,4'-BP monolayer, density functional theory (DFT) calculations in combination with SAMPLE³⁸ machine learning (ML) approach, based on Bayesian linear regression, were utilised. First, to identify energetically favourable adsorption geometries on Sb(111) surface, a lone 4,4'-BP molecule was placed at four different Sb(111) adsorption sites (top, bridge, hollow 1, hollow 2) and oriented at three different angles (0°, 45°, 90°, for bridge adsorption site; 0°, 15°, 30°, for other sites) relative to the direction perpendicular to Sb(111) surface. For more details see Figure S1 in Supplementary Information (SI). The adsorption geometries were relaxed to a minimum, with atomic forces below 0.05 eV/Å, while keeping Sb atoms fixed.

From the relaxed structures, 8 geometries with the highest adsorption energies were chosen for the SAMPLE approach to generate possible symmetry-unique monolayer configurations by combining different Sb(111) unit cells and given adsorption geometries. The studied monolayer structure unit cells had a minimum height of 2 primitive Sb(111) unit cells and contained up to 4 different local adsorption structures. The investigated surface concentration range of 4,4'-BP molecules was from 1.3×10^{-10} mol/cm² to 2.7×10^{-10} mol/cm² in the unit cells containing 1 and 2 different local structures and 2.0×10^{-10} mol/cm² to 2.7×10^{-10} mol/cm² with 3 and 4 different local 4,4'-BP adsorption structures. For the optimisation of hyperparameters, we made use of a training set consisting of 290 DFT single-point calculations of different SAM configurations, chosen using the D-optimality criterion, and a validation set consisting of 95 configurations. With optimised parameters, a root mean square error (RMSE) of adsorption energy of 0.085 eV per molecule was calculated. The hyperparameters used for the training of the model are provided in SI Table S1. To train the final model, used for the prediction of the surface structures, we used the optimised parameters and all 385 different SAM configurations. The final model was evaluated on a test set, made up of 45 previously unseen configurations, which gave RMSE of 0.10 eV per molecule. Using the trained model, the SAM configuration with the lowest adsorption energy per electrode surface area has been selected for further analysis.

All necessary DFT calculations were carried out using GPAW^{39–41} software package in LCAO mode, a grid spacing of 0.16 Å, dzp basis set, Perdew–Burke–Ernzerhof (PBE) exchange-correlation functional⁴², D4 dispersion correction⁴³ together with Brillouin-zone sampling with a minimum density of 14.5 points per Å⁻¹. The Sb(111) surface was created using experimental

lattice parameters⁴⁴ and not further relaxed to facilitate better comparability between STM and DFT results. Periodic boundary conditions were applied along the surface plane and dipole-layer correction in the nonperiodic direction perpendicular to the Sb(111) surface. In all calculations, the Sb(111) slab consisted of 4 layers (2 Sb bilayers), deemed a reasonable compromise between computation time and accuracy.

Results

The characterisation of the electrochemical behaviour of Sb(111) | 4,4'-BP + EMImBF₄ interface

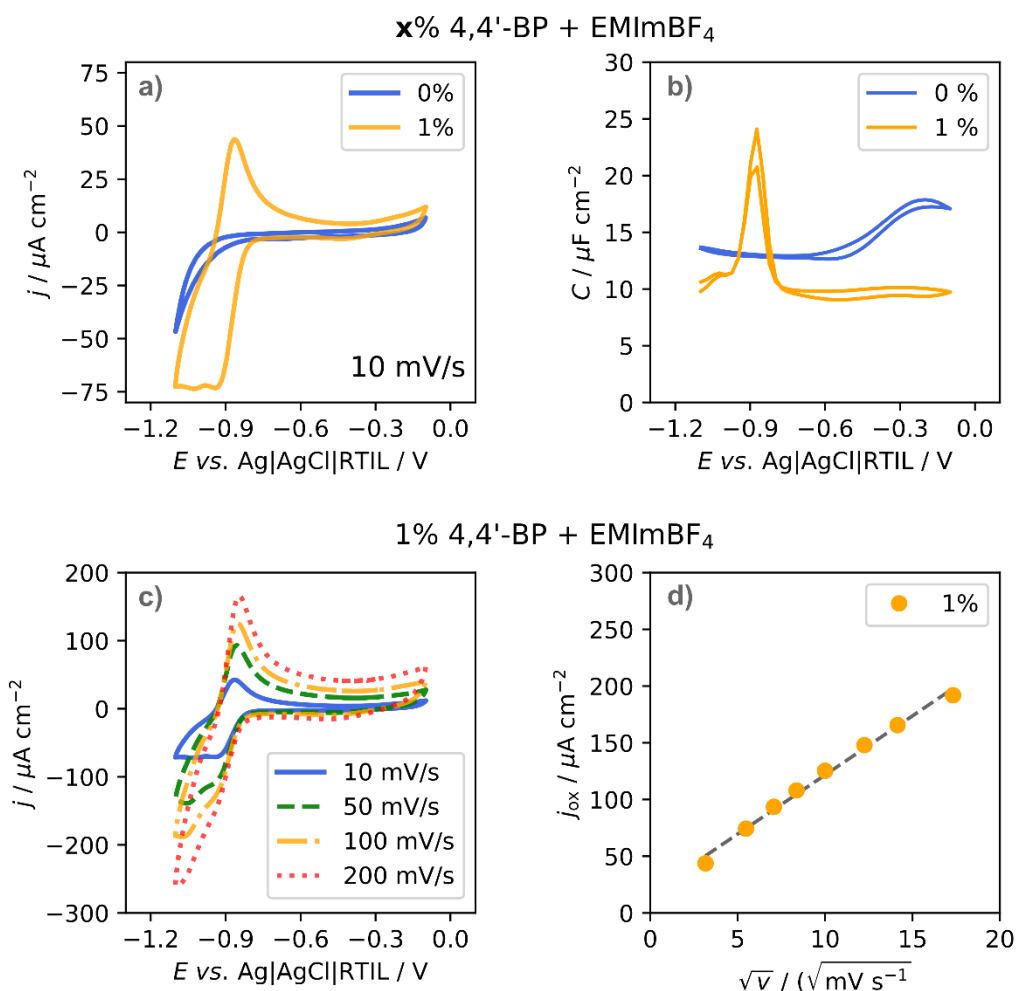


Figure 1. a) CVs at 10 mV/s scan rate; and b) differential capacitance (C) vs. potential (E) curves at 210 Hz for Sb(111) in EMImBF₄ and in 1.0 wt% 4,4'-BP + EMImBF₄; c) CVs at different potential scan rates for 1.0 wt% 4,4'-BP + EMImBF₄; d) Oxidation current (j_{ox}) dependence on potential scan rate (v) for 1.0 wt% 4,4'-BP + EMImBF₄.

The cyclic voltammograms (CVs) for Sb(111) in EMImBF₄ and 1.0 wt% 4,4'-BP + EMImBF₄ after electrochemical polishing are shown in Figure 1a in the potential range between $-1.1 \text{ V} < E < -0.1 \text{ V}$, first measured towards less negative E values and then towards more negative E values. During the potential scan in the negative direction, at $E < -0.7 \text{ V}$, the current decreases rapidly for EMImBF₄ solution with 4,4'-BP addition, indicating a reduction process (with a small peak at $E = -0.94 \text{ V}$) occurring at the interface. The charge transfer is pseudoreversible as the changing of the scan direction causes an oxidation peak at $E = -0.86 \text{ V}$. Described charge transfer process is not seen in the CVs of pure EMImBF₄, where the reduction current, related to the reduction of impurities such as water, starts to increase at $E < -0.95 \text{ V}$. Therefore, it can be related to the reduction of the adsorbed 4,4'-BP to 4,4'-BP⁻ in aprotic polar solvent⁴⁵. The process is also visible in the measured C vs. E dependences (Figure 1b) at 210 Hz. The C dependence of EMImBF₄ solution with 4,4'-BP addition has a noticeable peak at $E = -0.9 \text{ V}$, visible in both scanning directions, similarly to^{15,16}. This peak is not visible in the case of pure EMImBF₄ and its appearance suggests a reorganization process along with charge transfer occurring at the electrode's surface. In the range $-0.8 \text{ V} < E < -0.1 \text{ V}$, the capacitance curve has a plateau, which points to the adsorption and the formation of the compact layer of 4,4'-BP. When investigating the CVs at different potential scan rates for 1.0 wt% 4,4'-BP + EMImBF₄, given in Figure 1c, it is visible that the process is limited by the diffusion of 4,4'-BP due to the shifting of the oxidation peak with increasing scan rate. This is also confirmed by the linear dependence of the magnitude of the oxidation peak (j_{ox}) on the square root of the potential scan rate (\sqrt{v}), illustrated in Figure 1d.

Additional insight into the kinetics of interfacial processes can be gained using impedance modulus ($|Z|$) and Bode (phase angle, θ) plots (Figure 3). In the case of pure EMImBF₄, in the potential range between $-0.8 \text{ V} < E < -0.2 \text{ V}$, the interface has nearly ideal capacitive behaviour, with $\theta < -75^\circ$ in a large frequency range and the slope of $|Z|$ dependence, fitted in the f range between 0.1 Hz and 1000 Hz, being less than -0.86 , which is a slight deviation from the slope of -1.0 , characteristic of ideally polarizable interface⁴⁶. Only at low frequencies, small deviations of θ were observed, and they have been related to the slow reorganization of the IL at the interface with partial charge transfer between the IL's ions and the electrode^{25,47-50}. At lower potential values ($E < -0.9 \text{ V}$), the θ starts to increase, which points to the beginning of faradic processes, most likely the reduction of impurities (such as H₂O), which is in agreement with CVs in Figure 1a.

For the 1.0 wt% 4,4'-BP + EMImBF₄ solution, the phase angle dependencies show similar trends as the pure EMImBF₄ in the range $-0.6\text{ V} < E < -0.2\text{ V}$, although lacking the increase of θ at very low frequencies, possibly due to adsorbed 4,4'-BP molecules, which hinder the partial charge transfer between the Sb(111) and the IL ions. In the potential range between $-0.9\text{ V} < E < -0.6\text{ V}$ the θ increases, and a local maximum at $f \approx 10\text{ Hz}$ appears. A mixed kinetic process is visible, where the rate of the overall process is determined by the combination of diffusion, charge transfer and adsorption/desorption processes. The changes of phase angle dependence can be related to the reorganization of the adsorbed 4,4'-BP layers together with the charge transfer or reductive desorption of 4,4'-BP. Interestingly, at $E = -1.1\text{ V}$, the phase angle dependencies for both pure EMImBF₄ and for 1.0 wt% 4,4'-BP solution are very similar, without the θ maxima described above.

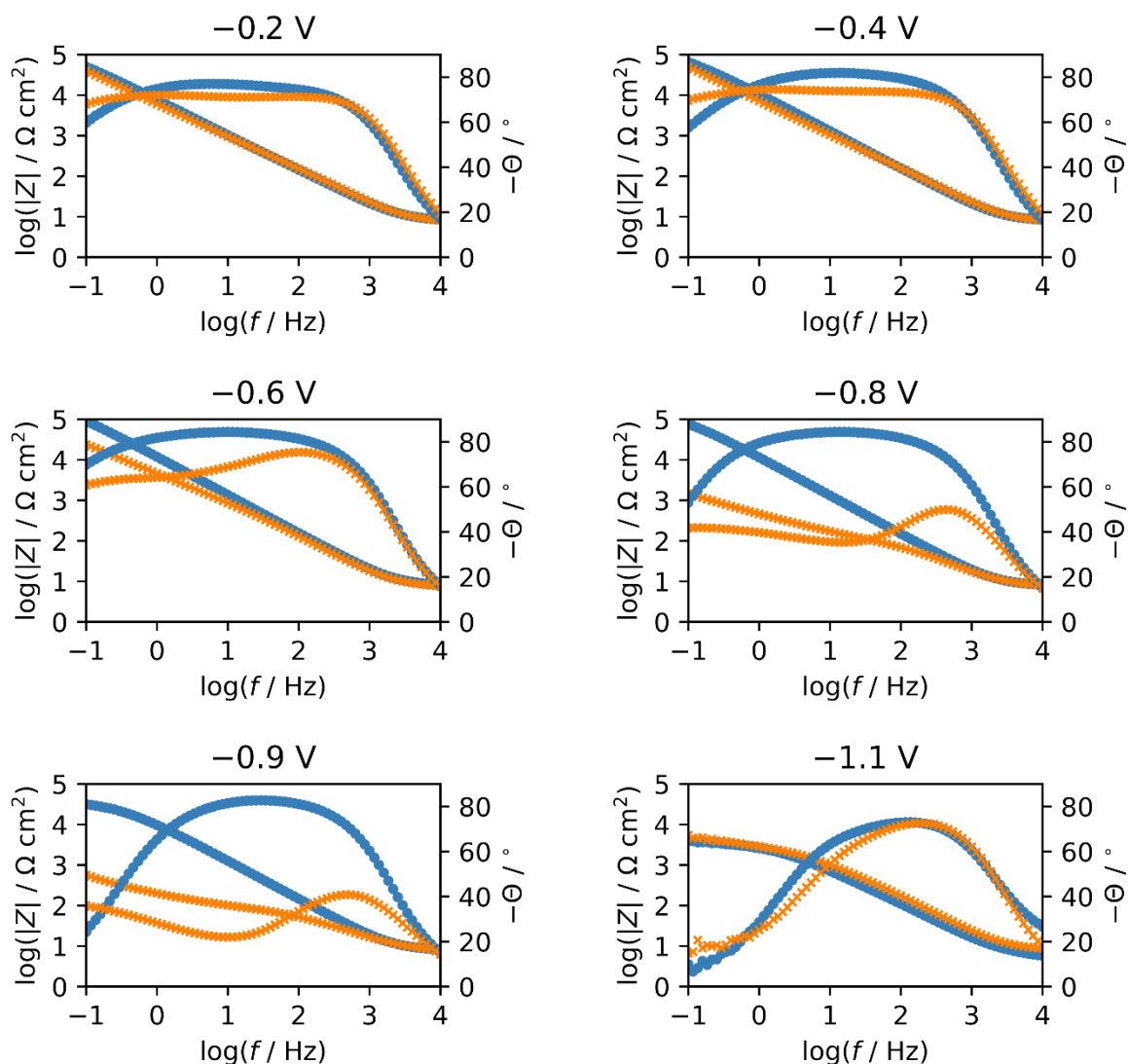


Figure 2. The impedance modulus ($|Z|$) and phase angle (θ) vs. $\log(\text{frequency})$ dependencies for Sb(111) in EMImBF₄ (blue) and 1.0 wt% 4,4'-BP + EMImBF₄ (orange) at chosen E values.

The formation of 4,4'-BP monolayers at the Sb(111) | 4,4'-BP + EMImBF₄ interface

The overall electrochemical behaviour of Sb(111) | 4,4'-BP + EMImBF₄ interface, described above using EIS and CV, hints at the possibility of the formation of compact 4,4'-BP adsorption layer due to large plateau together with a significant peak in C vs. E dependence. To study the orientation and distribution of 4,4'-BP on the Sb(111) surface at different applied potentials, *in*

situ STM measurements were conducted in the same E range as EIS and CV. Figure 3 illustrates the changing of the surface structure in the potential range $-0.9\text{ V} < E < -0.65\text{ V}$. The most distinct formation of ordered structure (Layer A) is observed at $E = -0.85\text{ V}$ and -0.75 V , where are clearly visible rows of 4,4'-BP molecules, interpreted to be oriented with the plane of aromatic rings parallel to the Sb surface, similarly to aqueous solution¹⁵. The formation of ordered 4,4'-BP arrangements was most pronounced when the E was changed towards less negative values due to the desorption of 4,4'-BP at $E < -0.85\text{ V}$. The ordered structure disappeared at $E > -0.75\text{ V}$, most probably due to further adsorption of 4,4'-BP, forming amorphous layers on top of the ordered layers on the Sb(111) surface. At $E = -0.9\text{ V}$, the ordered rows of Layer A disappear, as 4,4'-BP desorbs (shown in SI Figure S3), and a much more compact underlying structure is observed (Layer B). Although Layer B has denser structure, the distance between visible the rows, shown in Figure 3a, is too large to correspond to the interatomic distance between the two nearest Sb atoms ($a = 4.3\text{ Å}$ ⁴⁴) and therefore is likely consisting of strongly adsorbed 4,4'-BP molecules or 4,4'-BP⁻ ions. In addition to the ordered layers, the formation of bright clusters on the Sb(111) surface was also observed, similarly to Gorbatovski *et al.*¹⁵, which were related to the partial reduction and deposition of bipyridine on the electrode's surface.

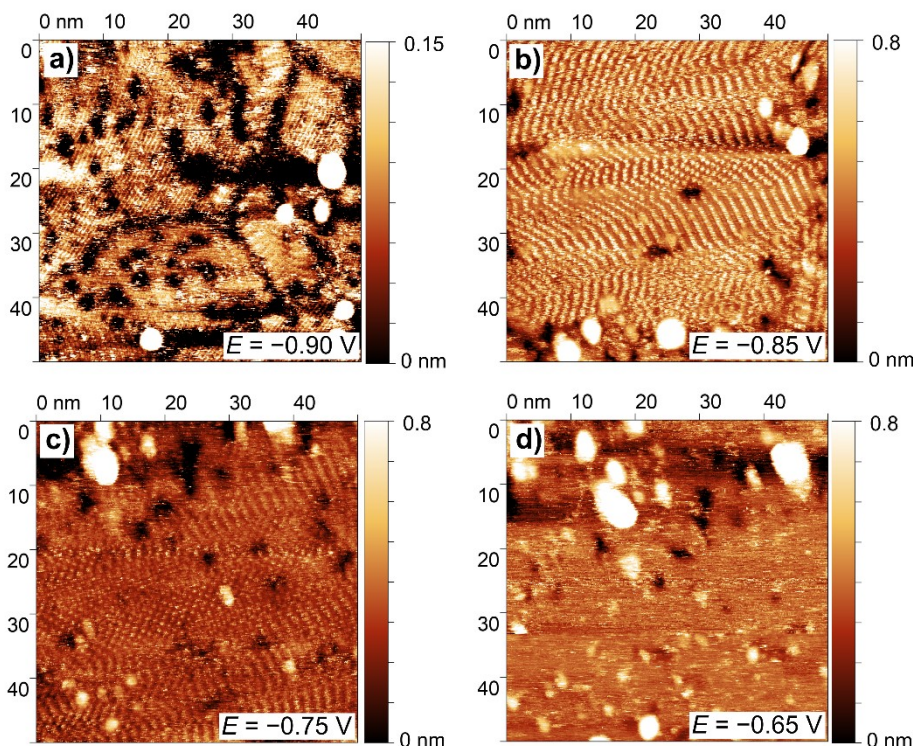


Figure 3. STM images of Sb(111) | 1% 4,4'-BP + EMImBF₄ interface at different potentials.

On the closer inspection of the periodic rows of Layer A, illustrated in Figure 4, two different patterns of 4,4'-BP were observed. The STM image of a first pattern (Pattern 1) is shown in Figure 4a together with the proposed unit cell. The unit cell of Pattern 1 contains one 4,4'-BP molecule and has a shape of a parallelogram with 4,4'-BP molecules at the corners. In Pattern 2, the 4,4'-BP molecules are packed more tightly in a row, with the distance between two molecules being reduced to 0.8 nm, while the distance between neighbouring rows remains the same. From the proposed unit cells, relatively low surface concentrations of 1.28×10^{-10} mol/cm² and 1.38×10^{-10} mol/cm² were estimated for patterns 1 and 2, respectively. The existence of multiple surface structures at similar potentials can be related to the defects in underlying Layer B or various configurations of 4,4'-BP molecules with similar interaction energies. The structure, characteristic of the Layer B, is illustrated in Figure 4c. Although the high density of the formed structure hindered the physical resolution of separate 4,4'-BP molecules and the determination of the measurements of the unit cell, the 4,4'-BP molecules, with pyridine rings visible, seem to be packed tightly to each other in ordered rows, without the space that was visible in surface structures belonging to Layer A.

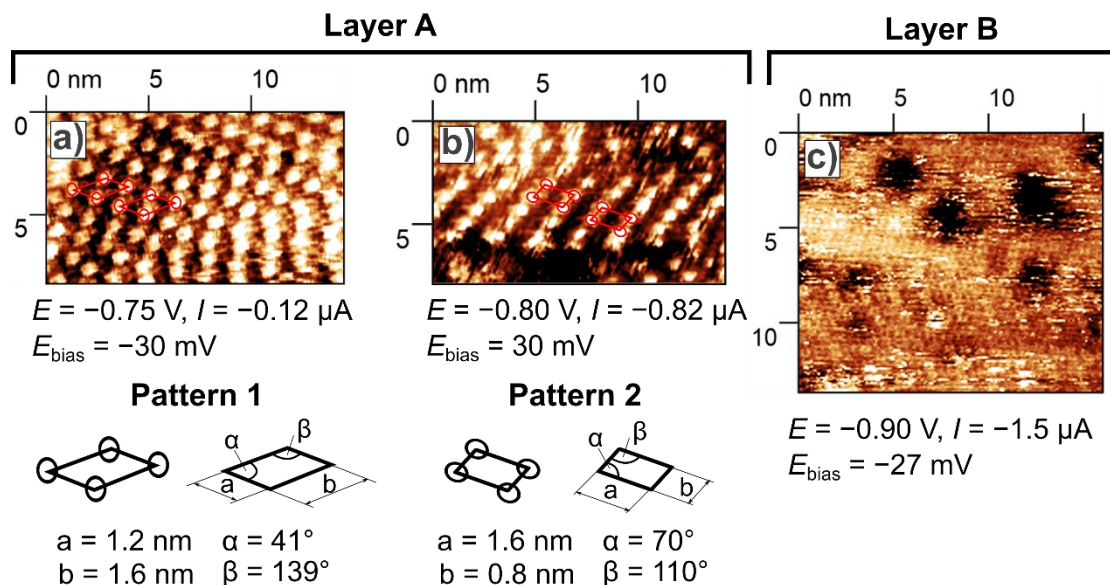


Figure 4. Different monolayer configurations, obtained from STM images of Sb(111) | 1.0% 4,4'-BP + EMImBF₄ interface together with proposed unit cells for configurations belonging to Layer A.

The computational modelling of Layer B and the interfacial structure

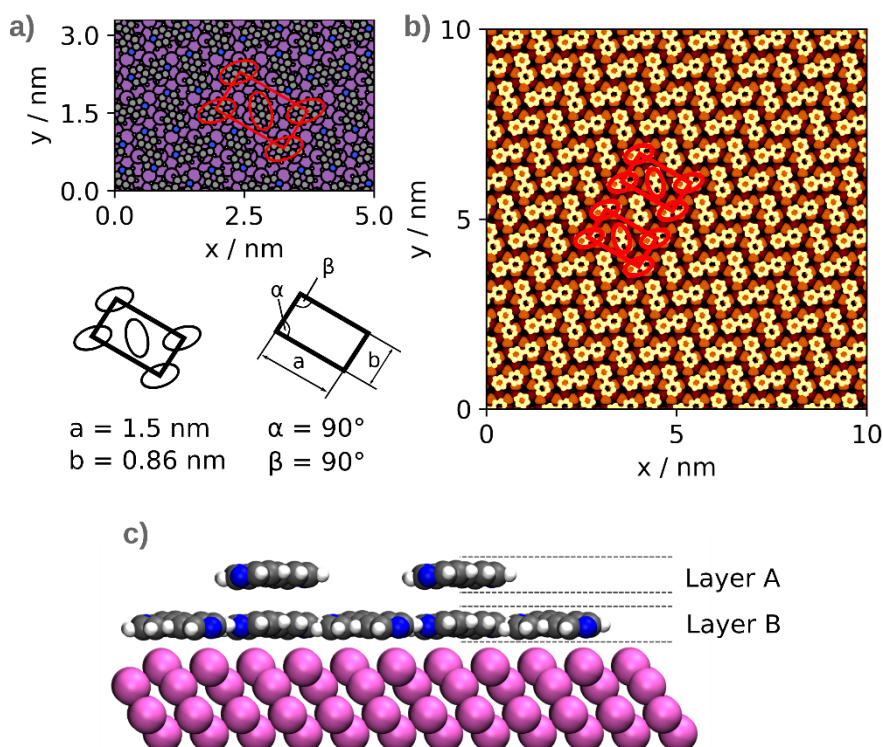


Figure 5. a) Monolayer configuration of 4,4'-BP molecules on Sb(111) surface together with a proposed unit cell of Layer B. b) Calculated STM image of Layer B. c) The model of organised 4,4'-BP multilayer structure on Sb(111) surface.

As the STM images indicated the existence of a tight underlying SAM layer, DFT calculations in combination with ML were used to evaluate the unit cell of Layer B. Figures 5a, and 5b show the predicted surface structure for layer B with the strongest adsorption energy per electrode surface area together with calculated STM image. The predicted surface structure for layer B consists of ordered 4,4'-BP rows, similar to experimental results. At the same time, the surface concentration of 2.58×10^{-10} mol/cm² was almost two times larger than determined for layer A. The 4,4'-BP molecules in the calculated layer B structure are positioned at the hollow 1 adsorption site. When comparing the 4,4'-BP adsorption energy that was predicted by the ML model with DFT calculations, they are in good agreement, being -1.34 eV and -1.37 eV, respectively. The molecules are oriented with the plane of aromatic rings parallel to the electrode's surface and interact with the Sb atoms through the π aromatic system. Interestingly, the adsorption energy of a 4,4'-BP molecule in the SAM structure is significantly more negative than for the isolated 4,4'-BP molecule (-0.66 eV, see Figure S4) at hollow 1 adsorption site, which underlines the importance of the interactions between the molecules in SAM. As the molecules are rotated relative to each other with nitrogen atoms pointed towards the centre of hydrogen atoms of the pyridine ring, in addition to dispersion forces, the formation of hydrogen bonds between 4,4'-BP molecules has a significant effect on the stabilisation of the structure, with the interaction being as strong as -0.23 eV for a pair of 4,4'-BP molecules. When comparing the unit cells of calculated layer B and measured layer A structures, it is apparent that the pattern 2 unit cell closely matches the layer B structure, with one additional 4,4'-BP molecule in the centre of the parallelogram. This allows concluding that the 4,4'-BP molecules of layer A are most likely situated on top of 4,4'-BP molecules of layer B with the empty space most likely filled by EMIm⁺ ions to screen the electrode's charge.

The formation of multi-layered ordered self-assembled structure of organic molecules adsorbed on the electrode | electrolyte interface, to the best of our knowledge, has not been previously reported, although, the existence of multilayer structure of IL ions at the interface have been previously shown in both experimental^{23,51,52} and computational studies^{50,53,54}. Furthermore, it has been shown that in ILs, if the ions form rigid layers on the electrode, it is necessary to apply an overpotential to replace the ions⁵⁵. In the case of electrolytes with organic molecules additives, the current understanding is that the highly ordered SAM structure does not extend beyond the first layer, directly in contact with the electrode's surface. This applies to the adsorption studies of 4,4'-BP¹²⁻¹⁶, 2,2'-BP^{34,56,57}, as well as other organic molecules forming organised layers⁵⁷⁻⁶⁰. The possibility of the existence of a possible denser SAM structure

underneath of a sparse monolayer is at the same time feasible if the molecules in the SAM can form hydrogen bond networks and adsorb strongly to the electrode's surface. The reasons why the underlying structure has not been previously reported can be explained by that the underlying denser structure is challenging to image with *in situ* STM and was only revealed as a result of the desorption in the current case. The existence of multiple self-assembled layers could have far-reaching ramifications for the applications, where the structure and properties of monolayer are essential, such as corrosion-resistant coatings⁶¹, single-molecule junctions and switches⁶², as well as other possible applications in nanoelectronics⁶³.

Conclusions

In this work, we investigated the properties of Sb(111) | 4,4'-BP + EMImBF₄ interface using *in situ* STM, EIS and DFT calculations. It was shown that reductive desorption of 4,4'-BP at Sb(111) surface occurred at $E < -0.8$ V. The capacitance dependence has a plateau when $E > -0.8$ V, which points to the adsorption of 4,4'-BP. The formation of 4,4'-BP SAMs was demonstrated with *in situ* STM, which showed that at least two ordered SAM structures are formed on top of each other at the Sb(111) surface. The first SAM layer, directly above the electrode's surface, consists of tightly packed ordered rows. Its fine structure and likely arrangement of 4,4'-BP molecules were estimated with machine learning in combination with DFT calculations, which predicted a configuration with a surface concentration of 2.58×10^{-10} mol/cm² where interactions between 4,4'-BP molecules have a significant effect on the adsorption energy. The second SAM layer had rather low estimated values of surface concentrations of 1.28×10^{-10} mol/cm² and 1.38×10^{-10} mol/cm² for two different structures. Although, the unit cells for the first SAM layer was obtained from the calculations and for the second SAM layer from the experiments, their measurements were in good agreement and allowed to propose a model of the structured SAM layers.

Acknowledgments

This work was supported by the Estonian Research Council grant PSG249 and by the EU through the European Regional Development Fund under project TK141 (2014-2020.4.01.15-0011). For providing us with the computational resources, we would like to acknowledge the HPC Center of the University of Tartu.

References

1. Casalini, S., Bortolotti, C. A., Leonardi, F. & Biscarini, F. Self-assembled monolayers in organic electronics. *Chem. Soc. Rev.* **46**, 40–71 (2017).
2. Ma, H., Yip, H.-L., Huang, F. & Jen, A. K.-Y. Interface Engineering for Organic Electronics. *Adv. Funct. Mater.* **20**, 1371–1388 (2010).
3. Ashurst, W. R., Yau, C., Carraro, C., Maboudian, R. & Dugger, M. T. Dichlorodimethylsilane as an anti-stiction monolayer for MEMS: a comparison to the octadecyltrichlorosilane self-assembled monolayer. *J. Microelectromech. Syst.* **10**, 41–49 (2001).
4. Kang, T. *et al.* Self-Assembled Monolayer Enables Slurry-Coating of Li Anode. *ACS Cent. Sci.* **5**, 468–476 (2019).
5. Singh, M., Kaur, N. & Comini, E. The role of self-assembled monolayers in electronic devices. *J. Mater. Chem. C* **8**, 3938–3955 (2020).
6. Novak, M. *et al.* Low-Voltage p- and n-Type Organic Self-Assembled Monolayer Field Effect Transistors. *Nano Lett.* **11**, 156–159 (2011).
7. Ulman, A. Formation and Structure of Self-Assembled Monolayers. *Chem. Rev.* **96**, 1533–1554 (1996).
8. Yamada, R., Sakai, H. & Uosaki, K. Solvent Effect on the Structure of the Self-Assembled Monolayer of Alkanethiol. *Chem. Lett.* **28**, 667–668 (1999).
9. Crivillers, N. *et al.* Large Work Function Shift of Gold Induced by a Novel Perfluorinated Azobenzene-Based Self-Assembled Monolayer. *Adv. Mater.* **25**, 432–436 (2013).
10. Chen, C.-Y. *et al.* Concomitant tuning of metal work function and wetting property with mixed self-assembled monolayers. *Org. Electron.* **12**, 148–153 (2011).

11. Karthäuser, S. Control of molecule-based transport for future molecular devices. *J. Phys.: Condens. Matter* **23**, 013001 (2010).
12. Mayer, D., Dretschkow, T., Ataka, K. & Wandlowski, T. Structural transitions in 4, 4'-bipyridine adlayers on Au (111)—an electrochemical and in-situ STM-study. *J. Electroanal. Chem.* **524**, 20–35 (2002).
13. Grozovski, V., Ivaništšev, V., Kasuk, H., Romann, T. & Lust, E. Balance of the interfacial interactions of 4, 4'-bipyridine at Bi (111) surface. *Electrochim. Acta* **120**, 86–95 (2014).
14. Diao, Y.-X. *et al.* Adsorbed structures of 4,4'-bipyridine on Cu(111) in acid studied by STM and IR. *Langmuir* **22**, 3640–3646 (2006).
15. Gorbatovski, G., Oll, O., Kasuk, H., Pikma, P. & Lust, E. In situ scanning tunneling microscopy study of bipyridine adsorption at semi-metallic Sb(111) plane. *Electrochem. commun* **105**, 106500 (2019).
16. Pikma, P. *et al.* Adsorption of 4,4'-bipyridine on the Cd(0001) single crystal electrode surface. *Electrochim. Acta* **180**, 965–976 (2015).
17. Galiński, M., Lewandowski, A. & Stepniak, I. Ionic liquids as electrolytes. *Electrochim. Acta* **51**, 5567–5580 (2006).
18. Tokuda, H., Hayamizu, K., Ishii, K., Susan, Md. A. B. H. & Watanabe, M. Physicochemical Properties and Structures of Room Temperature Ionic Liquids. 1. Variation of Anionic Species. *J. Phys. Chem. B* **108**, 16593–16600 (2004).
19. Tokuda, H., Hayamizu, K., Ishii, K., Susan, Md. A. B. H. & Watanabe, M. Physicochemical Properties and Structures of Room Temperature Ionic Liquids. 2. Variation of Alkyl Chain Length in Imidazolium Cation. *J. Phys. Chem. B* **109**, 6103–6110 (2005).

20. Shamsipur, M., Beigi, A. A. M., Teymouri, M., Pourmortazavi, S. M. & Irandoust, M. Physical and electrochemical properties of ionic liquids 1-ethyl-3-methylimidazolium tetrafluoroborate, 1-butyl-3-methylimidazolium trifluoromethanesulfonate and 1-butyl-1-methylpyrrolidinium bis(trifluoromethylsulfonyl)imide. *J. Mol. Liq.* **157**, 43–50 (2010).
21. Karu, K. *et al.* Predictions of Physicochemical Properties of Ionic Liquids with DFT. *Computation* **4**, 25 (2016).
22. Endres, F. & El Abedin, S. Z. Air and water stable ionic liquids in physical chemistry. *Phys. Chem. Chem. Phys.* **8**, 2101–2116 (2006).
23. Hayes, R. *et al.* Double Layer Structure of Ionic Liquids at the Au(111) Electrode Interface: An Atomic Force Microscopy Investigation. *J. Phys. Chem. C* **115**, 6855–6863 (2011).
24. Li, H., Endres, F. & Atkin, R. Effect of alkyl chain length and anion species on the interfacial nanostructure of ionic liquids at the Au(111)–ionic liquid interface as a function of potential. *Phys. Chem. Chem. Phys.* **15**, 14624–14633 (2013).
25. Siinor, L., Lust, K. & Lust, E. Electrical Double Layer Capacitance at Bi(111) | 1-Ethyl-3-methylimidazolium Tetrafluoroborate Interface as a Function of the Electrode Potential. *J. Electrochem. Soc.* **157**, F83–F87 (2010).
26. Siinor, L., Siimenson, C., Ivaništšev, V., Lust, K. & Lust, E. Influence of cation chemical composition and structure on the double layer capacitance for Bi(111) | room temperature ionic liquid interface. *J. Electroanal. Chem.* **668**, 30–36 (2012).
27. Rotenberg, B. & Salanne, M. Structural Transitions at Ionic Liquid Interfaces. *J. Phys. Chem. Lett.* **6**, 4978–4985 (2015).
28. Zhou, Y. & Qu, J. Ionic Liquids as Lubricant Additives: A Review. *ACS Appl. Mater. Interfaces* **9**, 3209–3222 (2017).

29. Somers, A. E., Howlett, P. C., MacFarlane, D. R. & Forsyth, M. A Review of Ionic Liquid Lubricants. *Lubricants* **1**, 3–21 (2013).
30. Mousavi, M. P. S. *et al.* Ionic Liquids as Electrolytes for Electrochemical Double-Layer Capacitors: Structures that Optimize Specific Energy. *ACS Appl. Mater. Interfaces* **8**, 3396–3406 (2016).
31. Lee, S.-Y. *et al.* Nonhumidified Intermediate Temperature Fuel Cells Using Protic Ionic Liquids. *J. Am. Chem. Soc.* **132**, 9764–9773 (2010).
32. Poole, C. F. & Poole, S. K. Extraction of organic compounds with room temperature ionic liquids. *J. Chromatogr. A* **1217**, 2268–2286 (2010).
33. Siinor, L., Siimenson, C., Lust, K. & Lust, E. Mixture of 1-ethyl-3-methylimidazolium tetrafluoroborate and 1-ethyl-3-methylimidazolium iodide: A new potential high capacitance electrolyte for EDLCs. *Electrochem. Commun.* **35**, 5–7 (2013).
34. Pikma, P., Siinor, L., Oll, O. & Lust, E. Formation of 2,2'-bipyridine adlayers at Sb(111)|ionic liquid+2,2'-bipyridine solution interface. *Electrochem. commun.* **61**, 61–65 (2015).
35. Newell, R., Faure-Vincent, J., Iliev, B., Schubert, T. & Aradilla, D. A new high performance ionic liquid mixture electrolyte for large temperature range supercapacitor applications (–70 °C to 80 °C) operating at 3.5V cell voltage. *Electrochim. Acta* **267**, 15–19 (2018).
36. Yao, G. *et al.* Evolution of Topological Surface States in Antimony Ultra-Thin Films. *Sci. Rep.* **3**, 2010 (2013).
37. Nečas, D. & Klapetek, P. Gwyddion: an open-source software for SPM data analysis. *Cent. Eur. J. Phys.* **10**, 181–188 (2012).

38. Hörmann, L., Jeindl, A., Egger, A. T., Scherbela, M. & Hofmann, O. T. SAMPLE: Surface structure search enabled by coarse graining and statistical learning. *Comput. Phys. Commun.* **244**, 143–155 (2019).
39. Mortensen, J. J., Hansen, L. B. & Jacobsen, K. W. Real-space grid implementation of the projector augmented wave method. *Phys. Rev. B* **71**, 035109 (2005).
40. Enkovaara, J. *et al.* Electronic structure calculations with GPAW: a real-space implementation of the projector augmented-wave method. *J. Phys.: Condens. Matter* **22**, 253202 (2010).
41. A. H. Larsen. Localized atomic orbital basis sets in the projector augmented wave method. (Technical University of Denmark, 2008).
42. Perdew, J. P., Burke, K. & Ernzerhof, M. Generalized Gradient Approximation Made Simple. *Phys. Rev. Lett.* **77**, 3865–3868 (1996).
43. Caldeweyher, E., Bannwarth, C. & Grimme, S. Extension of the D3 dispersion coefficient model. *J. Chem. Phys.* **147**, 034112 (2017).
44. Barrett, C. S., Cucka, P. & Haefner, K. The crystal structure of antimony at 4.2, 78 and 298° K. *Acta Crystallogr.* **16**, 451–453 (1963).
45. Brown, O. R. & Butterfield, R. J. Cathodic reductions of 2,2'-bipyridine and 4,4'-bipyridine in liquid ammonia. *Electrochim. Acta* **27**, 321–327 (1982).
46. Orazem, M. E., Pébère, N. & Tribollet, B. Enhanced Graphical Representation of Electrochemical Impedance Data. *J. Electrochem. Soc.* **153**, B129–B136 (2006).
47. Drüscler, M., Huber, B., Passerini, S. & Roling, B. Hysteresis Effects in the Potential-Dependent Double Layer Capacitance of Room Temperature Ionic Liquids at a Polycrystalline Platinum Interface. *J. Phys. Chem. C* **114**, 3614–3617 (2010).

48. Voroshylova, I. V. *et al.* Hysteresis in the MD Simulations of Differential Capacitance at the Ionic Liquid–Au Interface. *J. Phys. Chem. Lett.* 10408–10413 (2020)
doi:10.1021/acs.jpcclett.0c03212.
49. Siinor, L., Lust, K. & Lust, E. Influence of anion composition and size on the double layer capacitance for Bi(111)|room temperature ionic liquid interface. *Electrochemistry Communications* **12**, 1058–1061 (2010).
50. Ivaništšev, V. & Fedorov, M. V. Interfaces between Charged Surfaces and Ionic Liquids: Insights from Molecular Simulations. *Electrochem. Soc. Interface* **23**, 65–69 (2014).
51. Yokota, Y., Harada, T. & Fukui, K. Direct observation of layered structures at ionic liquid/solid interfaces by using frequency-modulation atomic force microscopy. *Chem. Commun.* **46**, 8627–8629 (2010).
52. Atkin, R. & Warr, G. G. Structure in Confined Room-Temperature Ionic Liquids. *J. Phys. Chem. C* **111**, 5162–5168 (2007).
53. Fedorov, M. V. & Kornyshev, A. A. Towards understanding the structure and capacitance of electrical double layer in ionic liquids. *Electrochim. Acta* **53**, 6835–6840 (2008).
54. Merlet, C., Salanne, M., Rotenberg, B. & Madden, P. A. Imidazolium Ionic Liquid Interfaces with Vapor and Graphite: Interfacial Tension and Capacitance from Coarse-Grained Molecular Simulations. *J. Phys. Chem. C* **115**, 16613–16618 (2011).
55. Motobayashi, K. *et al.* Potential-induced restructuring dynamics of ionic liquids on a gold electrode: Steric effect of constituent ions studied by surface-enhanced infrared absorption spectroscopy. *J. Electroanal. Chem* **800**, 126–133 (2017).
56. Siinor, L., Siimenson, C., Doneux, T. & Buess-Herman, C. Adsorption of 2,2'-bipyridine at an Au(111)|ionic liquid electrified interface. *Electrochem. Commun.* **78**, 56–59 (2017).

57. Kallip, S., Kasuk, H., Grozovski, V., Möller, P. & Lust, E. Adsorption of camphor and 2,2'-bipyridine on Bi(111) electrode surface. *Electrochim. Acta* **53**, 4035–4045 (2008).
58. Yasini, P. *et al.* Potential-Induced High-Conductance Transport Pathways through Single-Molecule Junctions. *J. Am. Chem. Soc* **141**, 10109–10116 (2019).
59. Li, Z., Han, B., Wan, L. J. & Wandlowski, Th. Supramolecular Nanostructures of 1,3,5-Benzene-tricarboxylic Acid at Electrified Au(111)/0.05 M H₂SO₄ Interfaces: An in Situ Scanning Tunneling Microscopy Study. *Langmuir* **21**, 6915–6928 (2005).
60. Han, B., Li, Z. & Wandlowski, T. Adsorption and self-assembly of aromatic carboxylic acids on Au/electrolyte interfaces. *Anal. Bioanal. Chem* **388**, 121–129 (2007).
61. Tasić, Ž. Z., Petrović Mihajlović, M. B., Radovanović, M. B. & Antonijević, M. M. New trends in corrosion protection of copper. *Chem. Pap.* **73**, 2103–2132 (2019).
62. Komoto, Y., Fujii, S., Iwane, M. & Kiguchi, M. Single-molecule junctions for molecular electronics. *J. Mater. Chem. C* **4**, 8842–8858 (2016).
63. Magomedov, A. *et al.* Self-Assembled Hole Transporting Monolayer for Highly Efficient Perovskite Solar Cells. *Adv. Energy Mater.* **8**, 1801892 (2018).